

Learning polycrystal plasticity using mesh-based subgraph geometric deep learning

Hanfeng Zhai^{1a}

^a*Department of Mechanical Engineering,
Stanford University, Stanford, 94305, CA, USA*

Abstract

Polycrystal plasticity in metals is characterized by nonlinear behavior and strain hardening, making numerical models computationally intensive. We employ Graph Neural Network (GNN) to surrogate polycrystal plasticity from finite element method (FEM) simulations. We present a novel message-passing GNN that encodes nodal strain and edge distances between FEM mesh cells, aggregates them to obtain embeddings, and combines the decoded embeddings with the nodal strains to predict stress tensors on graph nodes. We demonstrate training GNN based on subgraphs generated from FEM mesh-graphs, in which the mesh cells are converted to nodes and edges are created between adjacent cells. The GNN is trained on 72 graphs and tested on 18 graphs. We apply the trained GNN to periodic polycrystals and learn the stress-strain maps based on strain-gradient plasticity theory. The GNN is accurately trained based on FEM graphs, in which the R^2 for both training and testing sets are 0.993. The proposed GNN plasticity constitutive model speeds up more than 150 times compared with the benchmark FEM method on randomly selected test polycrystals. We also apply the trained GNN to 30 unseen FEM simulations and the GNN generalizes well with an overall R^2 of 0.992. Analysis of the von Mises stress distributions in polycrystals shows that the GNN model accurately learns the stress distribution with low error. By comparing the error distribution across training, testing, and unseen datasets, we can deduce that the proposed model does not overfit and generalizes well beyond the training data. This work is expected to pave the way for using graphs as surrogates in polycrystal plasticity modeling.

¹E-mail: hzhai@stanford.edu

Keywords: Polycrystal plasticity, Finite element method, Graph neural networks, Constitutive behavior

1. Introduction

Plasticity refers to the permanent deformation of solid materials under external load, of which has been researched for more than 100 years. The earliest efforts include works of von Mises [1] and Huber [2] to phenomenologically capture yield criteria. The post-yielding behavior is captured by the *flow* process, in which dislocation plays a significant role. Accurate predictions of plastic deformation are crucial for various practical applications, such as optimizing metal forming processes [3], designing materials with specific properties, e.g., fatigue resistance [4]), controlling semiconductor interconnects [5], and controlling metal 3D printing processes [6]. These applications demand accurate and efficient digital twins of crystal plasticity models.

Due to decades of effort in understanding plasticity, constructing the constitutive model for polycrystals is still an active and ongoing research area due to (1) There are various ways to pose plasticity mechanisms characterizing the plasticity features in continuum models such as temperature and rate dependence, anisotropy, etc. [7, 8, 9]. (2) By nature, plasticity is a multiscale problem, where numerous mechanisms contribute to the overall plastic behavior, such as single crystal dislocation [10], inter-grain friction [11], and grain boundary interactions [12], making it a challenging task to craft plasticity models integrate phenomena occurring at various scales; (3) The high computational expense associated with accurately simulating polycrystal plasticity using numerical methods such as finite elements [13, 14, 15]. The computational cost is mainly attributed to the path dependence and nonlinear nature of plasticity.

The recent developments of data-driven modeling for physical models could potentially task the high computational cost and surrogate plasticity models. In the subgrain scale, it has been shown that the stress-strain responses can be predicted using deep residual networks & dislocation characteristics [16], dislocation dynamics simulation data with combined neural networks and support vector machines [17]. Minkowski and Laurson combine molecular dynamics (MD) and convolutional neural networks (CNN) to predict sample-dependent yield stress and shear moduli [18]. Yang and Buehler [19] use GNN to predict stress, energy, and related properties on

graphs generated in MD simulations. Amigo et al. [20] use different regression methods to analyze the correlation between material parameters. Based on grain representations, Dai et al. [21] use graph neural networks (GNN) to predict the magnetic properties of polycrystalline graphs. Based on grain representations, Dai et al. [21] use graph neural networks (GNNs) to predict the magnetic properties of polycrystalline graphs. Using experimental data, mechanical responses can be predicted from 2D images of static structures and CNN [22]. Thomas et al. [23] use graph convolutional networks and combine experimental data to predict the mechanical properties of grains. In the continuum scale, Martinez and Hartmann [24] use CNN to predict stress-strain responses. Gladstone et al. [25] propose using GNN to learn mesh-based time-dependent PDEs.

This paper explores the possibilities of adopting data-driven methods to surrogate computational plasticity models. Taking advantage of open-source finite element models, we used *Neper* & *FEpX* to generate meshes and conduct numerical simulations of periodic polycrystals [26, 27]. The goal is to develop accurate and generalizable surrogate plasticity models based on finite element calculations. Developing such surrogate models has three main issues: (1) The generated finite element meshes have different degrees of freedom (DoF) for different polycrystal geometries. Traditional regression tools such as the Gaussian processes or neural networks mostly depend on a fixed number of training points. (2) The spatial connectivity between finite element mesh cells preserves important physical features, i.e., the physical properties are passed between adjacent mesh cells during the finite element calculations. It is difficult for matrix-based data to preserve such geometric features. (3) The data size is large. Each 10-grain polycrystal mesh contains \sim 10,000 mesh cells. Training on such data is an expensive task.

To tackle the first problem, we propose using GNN to handle data with different DoFs. Since GNN can be trained on graphs with different numbers of nodes & edges, meshes with different sizes can be potentially handled. This also helps us solve the second problem since GNN can handle the connectivity within the data. The connections between mesh cells preserve the spatial feature of the polycrystals. We generate graphs in which cells are converted to nodes where the adjacent cells are connected. To tackle the third problem, we propose training the GNN on subgraphs of finite element meshes. In fine, several novel approaches are proposed for tackling nonlinear plasticity surrogate modeling is presented.

The paper is arranged as follows: In Section 2 we present the formulation

of the crystal plasticity model and the data generation process. In Section 3 we present the mathematical model and training details of the message-passing GNNs, with the explanation of the details of subgraph training. In Section 4 we present the results of the predictions on training and testing sets, analysis of comparing GNN with finite element methods, and further deployment on unseen datasets. We briefly conclude the paper in Section 5.

2. Crystal plasticity

2.1. Model and problem formulation

Strain gradient crystal plasticity models are employed [28], in which we use the general theory following Han et al. and its corresponding implementation in *FEpX* [29, 27]. We begin with the deformation gradient tensor, defined as $\mathbf{F} = \frac{\partial \mathbf{x}}{\partial \mathbf{X}}$, can be decomposed into elastic and plastic parts:

$$\mathbf{F} = \mathbf{F}^e \mathbf{F}^p = \mathbf{v}^e \mathbf{r}^* \mathbf{F}^p \quad (1)$$

where the elastic gradient tensor can be decomposed to lattice rotation \mathbf{r}^* and elastic straining. \mathbf{F}^p pertains plastic slip. \mathbf{x} is the current configuration and \mathbf{X} is the reference configuration. The general schematic of the theory is illustrated in Figure 1.

The polycrystal motion is driven by stress σ . Under loading, the local form of the equilibrium equation writes:

$$\nabla \cdot \sigma + \mathbf{f} = 0 \quad (2)$$

where σ is the Cauchy stress (or simply termed “stress”). \mathbf{f} is the body force vector, in our implementation $\mathbf{f} = 0$. The relationship between the Cauchy stress and the shear stress writes:

$$\tau = (\det(\mathbf{v}^e)) \sigma \quad (3)$$

For elastic deformations, the stress-strain relationship can be expressed as the generalized Hooke’s law, which can be written as the

$$\sigma = \mathbb{C} \epsilon^e \quad (4)$$

where \mathbb{C} is the elastic moduli tensor (or stiffness tensor). $\mathbb{C} = [\mathcal{C}_{ij}]$ contains elastic constants to be specified in the simulation.

After yield, the stress contributes to plastic flow, which can be described by restricted slip. Here, $\hat{\mathbf{L}}^p$ is the plastic deformation gradient, which can be written in terms of the plastic slip:

$$\hat{\mathbf{L}}^p = (\dot{\mathbf{F}}^p) (\mathbf{F}^p)^{-1} \quad (5)$$

The Lagrangian strain tensor contains both the elastic and plastic contributions and can be expressed in terms of elastic and plastic strain gradient tensors:

$$\begin{aligned} \epsilon &= \frac{1}{2} \left(\mathbf{F}^{e\top} \mathbf{F}^e - (\mathbf{F}^p)^{-\top} (\mathbf{F}^p)^{-1} \right) \\ &= \epsilon^e + \epsilon^p \end{aligned} \quad (6)$$

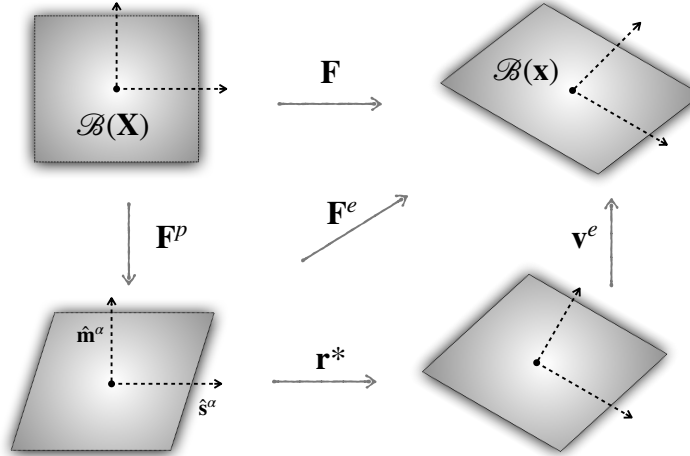


Figure 1: Schematic diagram for the decomposition in different configurations in crystal plasticity formulation. The visualization is inspired by Refs. [29, 27].

Using Schmid tensor's symmetric and skew part, the plastic deformation gradient in Eqn. (5) can be written in terms of slip using Schmid tensor's symmetric and skew parts:

$$\hat{\mathbf{L}}^p = \hat{\mathbf{D}}^{p'} + \hat{\mathbf{W}}^p \quad (7)$$

where

$$\hat{\mathbf{D}}^{p'} = \sum_{\alpha} \dot{\gamma}^{\alpha} \hat{\mathbf{p}}^{\alpha}, \quad \text{and} \quad \hat{\mathbf{W}}^p = (\dot{\mathbf{r}}^*) (\mathbf{r}^*)^{\top} + \sum_{\alpha} \dot{\gamma}^{\alpha} \hat{\mathbf{q}}^{\alpha} \quad (8)$$

Here, $\hat{\mathbf{p}}^\alpha$ and $\hat{\mathbf{q}}^\alpha$ are defined as

$$\begin{aligned}\hat{\mathbf{p}}^\alpha &= \hat{\mathbf{p}}^\alpha(\mathbf{q}) = \mathbf{sym}(\hat{\mathbf{s}}^\alpha \otimes \hat{\mathbf{m}}^\alpha) \\ \hat{\mathbf{q}}^\alpha &= \hat{\mathbf{q}}^\alpha(\mathbf{q}) = \mathbf{skw}(\hat{\mathbf{s}}^\alpha \otimes \hat{\mathbf{m}}^\alpha)\end{aligned}\quad (9)$$

where $\hat{\mathbf{s}}^\alpha$ and $\hat{\mathbf{m}}^\alpha$ are the slip directions obtained after the kinetic decomposition visualized in Figure 1. Note that the symmetric and skew parts are expressed as:

$$\begin{aligned}\mathbf{sym}(\cdot) &= \frac{1}{2} [(\cdot) + (\cdot)]^\top \\ \mathbf{skw}(\cdot) &= \frac{1}{2} [(\cdot) - (\cdot)]^\top\end{aligned}\quad (10)$$

$\dot{\gamma}^\alpha$ is the slip system shearing rate. Here, the shearing rate relates to the resolved shear stress τ^α via an assumed power law relationship:

$$\dot{\gamma}^\alpha = \dot{\gamma}_0 \left(\frac{|\tau^\alpha|}{g^\alpha} \right)^{\frac{1}{m}} \mathbf{sgn}(\tau^\alpha) \quad (11)$$

where $\dot{\gamma}_0$ is the fixed-rate strain rate scaling coefficient, m is the rate sensitivity exponent. The resolved shear stress τ^α is the projection of the crystal stress tensor onto the slip plane (in that particular slip direction) obtained via the Schmid tensor's symmetric part (Eqn. (9)):

$$\tau^\alpha = \mathbf{tr}(\hat{\mathbf{p}}^\alpha \tau') \quad (12)$$

The evolution of slip system strength g^α can be characterized by hardening modulus h_0 and the initial strengths following a power law:

$$\dot{g}^\alpha = h_0 \left(\frac{g_s(\dot{\gamma}) - g^\alpha}{g_s(\dot{\gamma}) - g_0} \right)^n \dot{\gamma} \quad (13)$$

where n is the nonlinear Voce hardening exponent. $g_s(\dot{\gamma})$ is the initial slip system saturation strength. g_0 is the initial slip system strength. $\dot{\gamma}$ is calculated as the summation of the slip shearing rates, related to resolved shear stresses (Eqn. (11)):

$$\dot{\gamma} = \sum_\alpha |\dot{\gamma}^\alpha| \quad (14)$$

The boundary conditions (B.C.s) can be specified via

$$\mathbf{v}(\mathbf{x}) = \bar{\mathbf{v}} \quad (15)$$

as the velocity B.C.s. In our implementation in *FEpX* [27], we apply fixed strain rate in x -direction, $\dot{\epsilon}_{xx} = 10^{-3} \text{ s}^{-1}$, which only acts on the v_z components. The applied strain rates in other directions are all set to be zero.

2.2. Material parameters & data generation

The rate sensitivity exponent in Eqn. (11) is set to be $m = 0.02$. We employ an isotropic hardening type. The fixed-rate strain rate is $\dot{\gamma}_0 = 1$. The simulation targets a total strain of $\epsilon_{xx} = 0.01$, implemented in a single deformation step with a strain increment of 0.001. We generate 90 10-grain periodic polycrystals, in which the mesh is generated via *Neper* [26]. We used BCC crystals with elastic constants $C_{11} = 236.9$ [GPa], $C_{12} = 140.6$ [GPa], and $C_{44} = 116.0$ [GPa]. The hardening modulus $h_0 = 391.90$ [MPa] and the slip strengths are $g_0 = 200$ & $g_s = 335$ [MPa], respectively. The nonlinear Voce hardening exponent is $n = 1$. The 90 simulation results are then converted to graphs, of which 72 graphs are selected for the training and the remaining 18 graphs are considered as the testing sets. See Ref. [27, 30] for details and related finite element implementation.

In our formulation, we hypothesize that the finite element meshes can be formulated as a graph $\mathcal{G} = \mathcal{G}(V, E)$, where $V \in \mathbb{R}^N$ & $E \in \mathbb{R}^M$ are vertices and edges of the graph, where $V = V(\epsilon_i \rightarrow \sigma_i)$ are the node features (on the finite element mesh node i) and $E = E(\ell_{ij})$ (Euclidean distances of mesh cells, on edge $i-j$ that connects nodes i & j). M & N are the number of edges and nodes. Each cell of the finite element mesh is considered a node. The edges are constructed according to the connectivity of the nodes. Here, we aim to learn the nodal map from total strain to stress, i.e., $\mathfrak{M} : \epsilon \in \mathbb{R}^6 \rightarrow \sigma \in \mathbb{R}^6$. We want to use the GNN to surrogate the model \mathfrak{M} . The overall stress-strain map for the physics-based model can be simplified in a form:

$$\sigma_i^{FEM} \equiv \sigma_i(\mathbf{x}) = \mathfrak{M}([\epsilon_i(\mathbf{x}), \mathbf{F}]; \mathbf{p}) \quad (16)$$

where $\mathbf{p} = (\mathbb{C}, g_0, g_s, h_0, m, n, \dots)$ subsumes all the related material parameters used in the simulation. The model $\mathfrak{M}(\cdot)$ takes strain ϵ_i and the configurational map \mathbf{F} , and \mathbf{p} as input and predict stress σ_i according to the equations presented above.

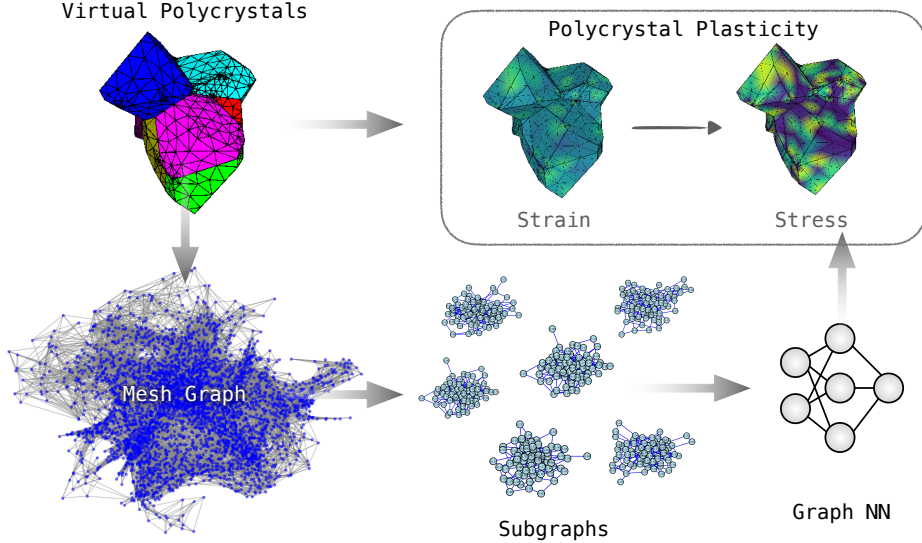


Figure 2: General schematic of the workflow for using GNN to learn polycrystal plasticity. Virtual polycrystals are generated using *FEpX*. It is converted to mesh graphs based on finite element cells. The subgraphs are extracted to train the GNN. The GNN is then deployed to surrogate polycrystal plasticity simulations.

In Eqn. (16), σ_i contains six stress elements under the Voigt notation in which they are defined as $\{\sigma_1, \sigma_2, \sigma_3, \sigma_4, \sigma_5, \sigma_6\} \equiv \{\sigma_{11}, \sigma_{12}, \sigma_{13}, \sigma_{22}, \sigma_{23}, \sigma_{33}\} \in \mathbb{R}^6$ (same for the strain components) for the overall stress & strain tensor elements in the finite element implementation.

3. Message-passing graph neural networks

3.1. Message-passing on edges for nodal inference

Message-passing GNN learns the data relationship on graphs by passing the message from edges to nodes (vertex) and conducting nonlinear regression (using MLP) in the feature space. One begins with preparing the “messages” on edges, where the accumulated nodal message $\tilde{\mathcal{M}}_{ij}^\epsilon$ (on edge) and edge message $\tilde{\mathcal{M}}_{ij}^\ell$ for edge $i-j$ can be written as:

$$\tilde{\mathcal{M}}_{ij}^\epsilon = \text{MSG}^{(n)}(\{\epsilon_i^{in}, \epsilon_j^{in}\}), \quad \tilde{\mathcal{M}}_{ij}^\ell = \text{MSG}^{(e)}(\{\ell_{ij}\}) \quad (17)$$

Here, we have $\tilde{\mathcal{M}}_{ij}^\epsilon \in \mathbb{R}^{M \times 6}$ (passing the information of strains ϵ) and $\tilde{\mathcal{M}}_{ij}^\ell \in \mathbb{R}^{M \times 1}$ (information of Euclidean distances ℓ). Here, 6 and 1 are the feature

space dimensions for nodes and edges. ϵ_i^{in} and ϵ_j^{in} are the nodal strains (input property) for nodes i & j ; and ℓ_{ij} are the edge input property, i.e., the mesh link length of edge $i-j$.

The nodal end edge messages are passed to the embedding dimension via two separate MLPs and output $\mathbf{h}_{ij}^{(n)}$ and $\mathbf{h}_{ij}^{(e)}$ with dimension $\mathbb{R}^{M \times emb}$. In our implementation $emb = 31$. The predicted embedding output is then concatenated into $\tilde{\mathbf{h}}_{ij}$, with dimension $\mathbb{R}^{M \times (2emb)}$, and the output is then fed into the decoding MLP to obtain $\tilde{\mathcal{E}}_{ij}$:

$$\begin{aligned} \mathbf{h}_{ij}^{(n)} &= \text{MLP}^{(N-ENC)}(\tilde{\mathcal{M}}_{ij}^{\epsilon}), & \mathbf{h}_{ij}^{(e)} &= \text{MLP}^{(E-ENC)}(\tilde{\mathcal{M}}_{ij}^{\ell}), \\ \tilde{\mathbf{h}}_i^{(n)} &= \bigoplus_{j \in \mathcal{N}(i)} \left(\left\{ \mathbf{h}_{ij}^{(n)} \right\} \right), & \tilde{\mathbf{h}}_i^{(e)} &= \bigoplus_{j \in \mathcal{N}(i)} \left(\left\{ \mathbf{h}_{ij}^{(e)} \right\} \right) \end{aligned} \quad (18)$$

where $\tilde{\mathcal{E}}_{ij} \in \mathbb{R}^{M \times 1}$, which can be considered as the decoded inference being done on the edges. $\mathcal{N}(i)$ stands for the neighboring node list for node i . To pass the prediction on nodes, aggregation is being conducted for the decoded information in the message-passing layer \mathcal{E}_{ij} :

$$\Xi_i = \text{MLP}^{(DEC)} \left(\left\{ \tilde{\mathbf{h}}_i^{(n)}, \tilde{\mathbf{h}}_i^{(e)} \right\} \right) \quad (19)$$

where \bigoplus_j is the aggregation operator that sums over the neighboring node and edge information for node i . This process is the *message-passing* from edges to nodes. This aggregation is being done in the embedding dimension and the output $\Xi_i \in \mathbb{R}^{N \times 1}$ is the properties on the node. The prediction follows an “equation-MLP” using the given nodal information and decoded edge information (on the node):

$$\tilde{\sigma}_i = \text{MLP}^{(EQN)} \left(\left\{ \epsilon_i^{in}, \Xi_i \right\} \right) \quad (20)$$

where $\tilde{\sigma}_i \in \mathbb{R}^{N \times 6}$ are the final stress predictions for the supervised learning target, which is the optimization goal $\tilde{\sigma}_i \sim \sigma_i$.

The training uses mean-squared error (MSE) as the objective \mathcal{L} parameterized by trainable variables Θ for supervised training. The optimization problem writes:

$$\begin{aligned} &\arg \min_{\Theta} \mathcal{L}(\Theta), \\ \mathcal{L} &= \frac{1}{\dim(\sigma)} \sum_{i \in \dim(\sigma)} (\tilde{\sigma}_i - \sigma_i)^2 \end{aligned} \quad (21)$$

where MSE is being calculated on all the nodes on the graph, $\dim(\sigma) = \mathbb{N}$.

To summarize, from Eqn. (17)-(20), the overall model can be simplified as a surrogate model for the ϵ - σ map:

$$\sigma_i^{GNN} \equiv \tilde{\sigma}_i = \gamma \left(\epsilon_i^{in}, \bigoplus_{j \in \mathcal{N}(i)} \phi \left(\left\{ \epsilon_i^{in}, \epsilon_j^{in} \right\}, \ell_{ij} \right) \right) \quad (22)$$

where γ and ϕ represent (combination of) different MLPs. This formula follows the generalized formula for message-passing GNN. The prediction is estimated based on the comparison of stresses predicted by GNN and FEM denoted in Eqns. (16) and (22).

3.2. Model framework & training

Figure 3 illustrates the general architecture of our message-passing GNN. The node and edge-encoding layer takes in the nodal and edge properties on edge $i-j$, and output $\mathbf{h}_{ij}^{(n)}$ and $\mathbf{h}_{ij}^{(e)}$, which are then passed to aggregation to pass the properties from edges to nodes to obtain $\tilde{\mathbf{h}}_i^{(n)}$ and $\tilde{\mathbf{h}}_i^{(e)}$ in the embedding dimension (Eqn. (18)). The concatenated output $\{\tilde{\mathbf{h}}_i^{(n)}, \tilde{\mathbf{h}}_i^{(e)}\}$ ($\in \mathbb{R}^{\mathbb{N} \times 2\text{emb}}$) is then sent to the decoding layer to $\Xi_i \in \mathbb{R}^{\mathbb{N} \times 1}$. Ξ_i and node input property ϵ_i are then being concatenated and input to the equation layer to give the prediction that aims to approximate σ_i (Eqn. (20)). The subscripts $(\cdot)_{mn}$ denote the elements in the stress & strain tensors, and $(\cdot)_{ij}$ denotes the connection of nodes in graphs.

3.2.1. Subgraph sampling

We propose training GNN on subgraphs to learn the mapping. Let $\mathcal{G}^{\text{sub}} = \mathcal{G}^{\text{sub}}(V^{\text{sub}}, E^{\text{sub}})$ denote the subgraph extracted from the full graph \mathcal{G} with randomly selected nodes, where $V^{\text{sub}} \subseteq V$ & $E^{\text{sub}} \subseteq E$. Within V^{sub} , let \hat{V}^{sub} be all the subgraph nodes that preserve full edges compared with \mathcal{G} . $\hat{V}^{\text{sub}} \cap V^{\text{sub}}$ are the nodes that lose edges during the subgraph extraction process. Each finite element mesh graph contains $\sim 10^5$ nodes in our implementation. For effective and efficient training of GNN, we propose training GNN on the subgraph, in which only the \hat{V}^{sub} and the connected edges are considered in the loss calculation, $\mathcal{L} = \text{MSE}(\mathcal{G}^{\text{sub}}(\hat{V}^{\text{sub}}))$. \hat{V}^{sub} can be selected by comparing the number of edges per node of \mathcal{G}^{sub} and \mathcal{G} (based on the global node index). The filtered node indices (connection indices) are denoted as \mathbf{c}^{ind} . One then uses \mathbf{c}^{ind} to select “active nodes” to put into the loss function.

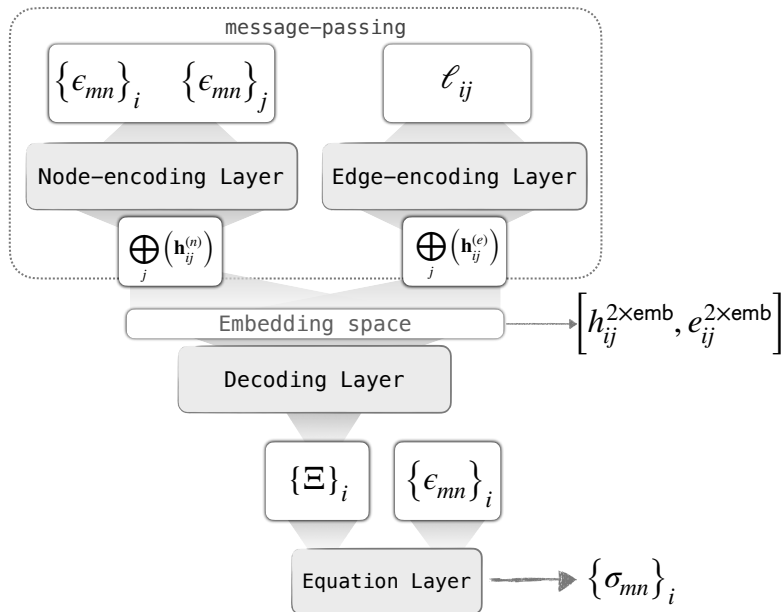


Figure 3: The general architecture for the GNN. The node-encoding layer takes the strains on neighboring nodes for the input edges, and the edge-encoding layer takes the mesh cell link length (i.e. Euclidean norm of mesh cells). The combined outputs are then fed into the embedding space ($\text{EMB} \in \mathbb{R}^{2 \times \text{emb}}$). The output EMB are then fed into the decoding layer that maps $\mathbb{R}^{2 \times \text{emb}}$ to \mathbb{R}^4 . The output of the decoding layer is then passed to the message-passing operator (i.e. \bigoplus), where the decoded messages are passed on nodes. The edge information on nodes $\{\epsilon_{mn}\}_i$ are then combined to put into the equation layer, to predict the corresponding stress components $\{\sigma_{mn}\}_i$.

3.2.2. Training algorithm

The training algorithm is shown in Algorithm 1. Finite element mesh-based graphs are stored in the form of `Torch Geometric` tensors, containing nodal (ϵ & σ) and edge properties (ℓ). Subgraphs are extracted based on the training ratio ξ_{train} , specifying the ratio of the number of nodes selected from the full graph \mathcal{G} . We use $\xi_{\text{train}} = 0.5$ for our training. We pre-sample a set of subgraphs in the training set for each iteration and prepare a list of sampled subgraphs \mathcal{B}_G for training implementation. Under each iteration, the unique subgraph sets per that iteration will be selected, in which the active nodes are selected based on \mathbf{c}^{ind} and fed into the loss function (21). Adam optimizer is selected for gradient-based optimization. The model is being trained on the 72 graphs for 1000 iterations.

Algorithm 1 Training algorithms for message-passing GNN

Require: Graph data files containing $\mathcal{G}(V, E)$ converted from finite element meshes, stored in the form of `Torch Geometric` tensors; mapping the nodal input to outputs $\epsilon \in \mathbb{R}^{N \times 6} \oplus \ell \in \mathbb{R}^{M \times 1} \mapsto \sigma \in \mathbb{R}^{N \times 6}$.

Hyperparameters: Training ratio: ξ_{train} ; The embedding dimension `emb`; Number of iterations `Itr`; Select optimizer `Adam`(\cdot); pre-sampled subgraphs list $\mathcal{B}_G(\text{Itr})$ from the training graphs.

Load pretrained GNN model $\mathcal{M}_G[\cdot]$. ▷ optional based on existence

for $itr < \text{Itr}$ **do**

$\mathcal{G}^{\text{sub}} \leftarrow \mathcal{B}_G(itr)$ ▷ obtain pre-sampled subgraph

$\mathbf{c}^{\text{ind}} \leftarrow \mathcal{F}(\mathcal{G}^{\text{sub}}, \mathcal{G})$. ▷ $\mathcal{F}(\cdot)$: filtering function to sort connection indices

$\tilde{\sigma} \leftarrow \mathcal{M}_G[\mathcal{G}^{\text{sub}}(\epsilon, \ell)]$ ▷ based on defined GNN in Sec. 3.2.

$\mathcal{L} \leftarrow \text{MSE}(\tilde{\sigma}[\mathbf{c}^{\text{ind}}], \sigma[\mathbf{c}^{\text{ind}}])$ ▷ only active nodes are included in the loss.

$\mathcal{M}_G(\Theta) \xleftarrow{\text{backward}} \mathcal{L}$. ▷ backpropagation

 Clips gradient norm, & optimization: $\arg \min_{\Theta} \mathcal{L}$. ▷ Adam(\cdot)

end for

Save the trained GNN model \mathcal{M}_G . ▷ requires the specified device for testing.

4. Results and discussions

4.1. Training and testing results

Figure 4 displays the overall results of the model training and testing. The left subfigure shows the prediction evaluations on the training set, while

the right subfigure shows the prediction evaluations on the testing set. Both subfigures illustrate a high degree of correlation between the predicted and benchmark values, with R^2 values of 0.993 and Pearson correlation coefficients of 0.996. The red dashed lines represent the ideal “ $y = x$ ” line, indicating predictions equal to benchmark values. The insets in each subfigure show the mean absolute error (MAE) distributions, further highlighting the model’s performance. These results demonstrate the model’s strong predictive accuracy on both training and testing datasets.

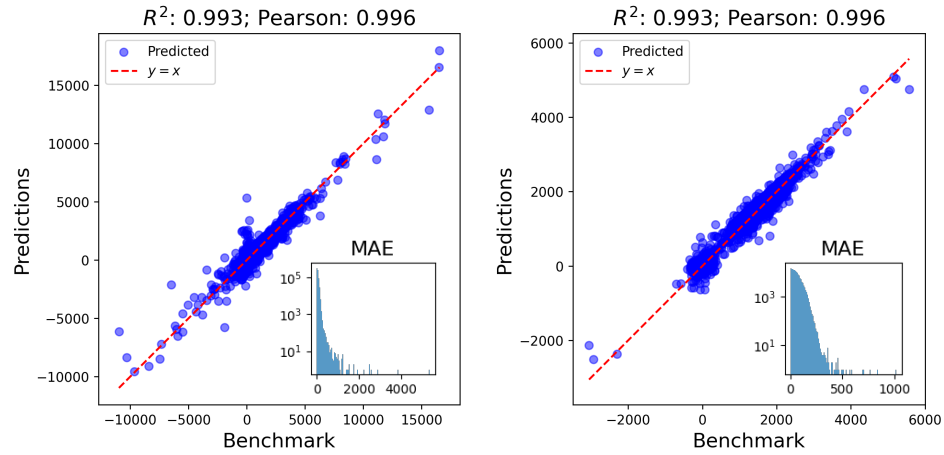


Figure 4: The predictions of the trained model on the training & test sets for all the stress components. The left subfigure is the prediction on the training set and the right subfigure is on the testing set. The distribution of MAE is then visualized in the right-bottom corners.

Accompanying the high R^2 values, to directly verify the high-quality predictions using GNN, the stress values on each finite element cell for both training and testing sets are visualized (Figure 5). The general data trends are well captured. With von Mises’s stress as label marks, the predictions preserve the stress distribution among mesh cells for both the training and test sets, indicating no overfitting for the proposed method. Since the loading is applied in the “1-direction”, Further visualizations for $\epsilon_1 - \sigma_1$ maps are presented for training and testing sets (Figure 6). The “loading map” is well learned by the GNN, from the predicted data trends. With the similar high-level preservation of the data trends, it is shown that GNN does not overfit the training set. Overall, Figures 4-6 demonstrate the quality of the predictions with direction prediction data visualization and high R^2 scores.

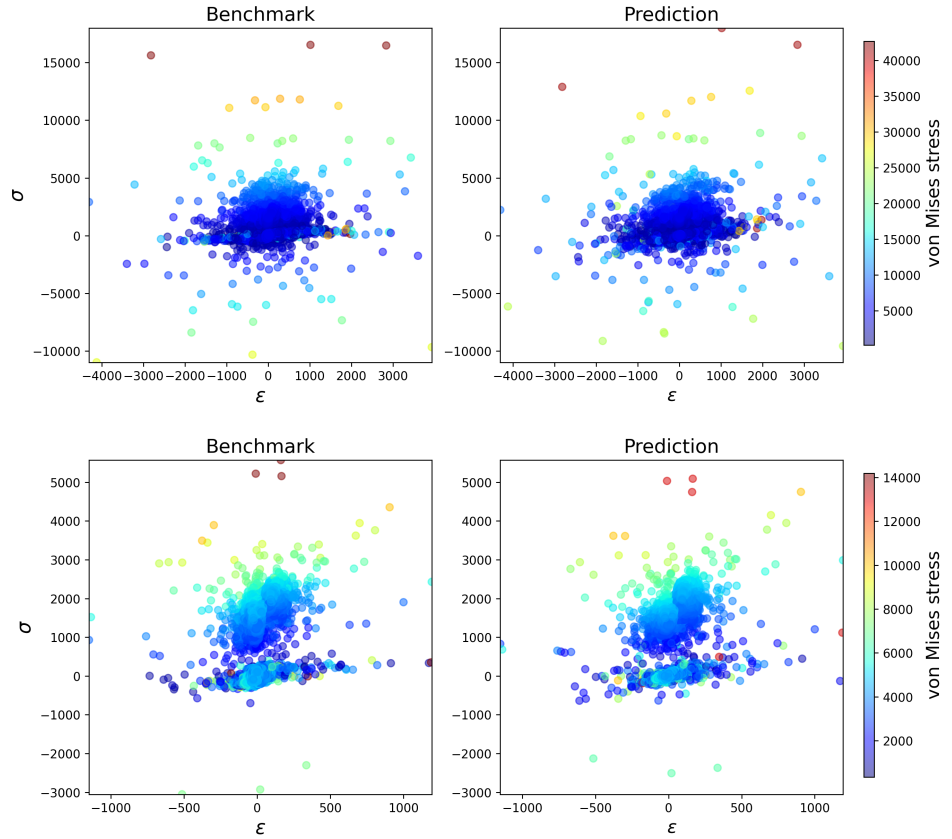


Figure 5: The comparison between the ground truth (by *FEpX*) and predictions on the stress-strain maps for all the stress & strain components. The upper figures correspond to the training sets. The bottom figures correspond to the testing sets. The data points are visualized according to the calculated von Mises stresses.

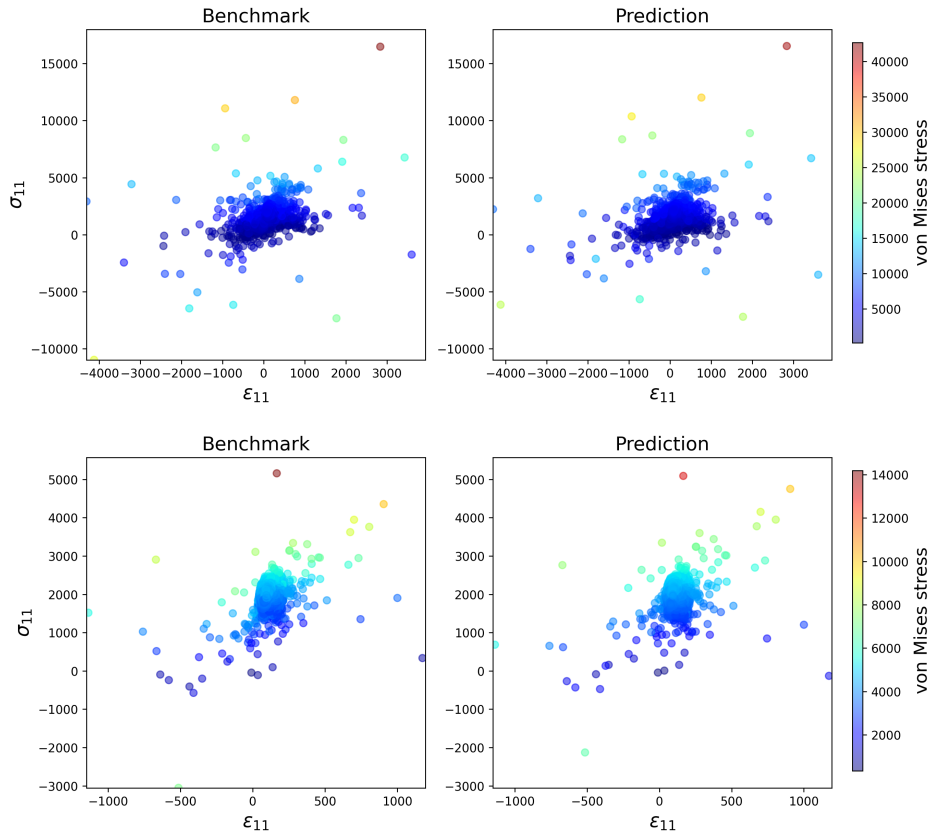


Figure 6: The comparison between the ground truth (by *FEpX*) and predictions on the stress-strain maps on 1-direction (i.e., $\epsilon_{11} \rightarrow \sigma_{11}$). The upper figures correspond to the training sets. The bottom figures correspond to the testing sets. The data points are visualized according to the calculated von Mises stresses.

4.2. Analysis on finite element meshes

Accompanying with the data visualization (Figures 5 & 6), we directly visualize the stress distributions on the virtual polycrystals (Figures 7 & 8) for a test polycrystal with R^2 of 0.994. Data scales are well captured by the GNN for each stress component σ_i , with comparably small absolute errors (Figure 7). By observation, the GNN is able to distinguish the active loading directions by learning different stress value ranges for each component, considering such constraints are not imposed or provided to the GNN *a priori*. Specifically, the stresses coupled with the loading direction ($\sigma_1 \sim \sigma_3$) are observable higher than the rest ($\sigma_3 \sim \sigma_6$).

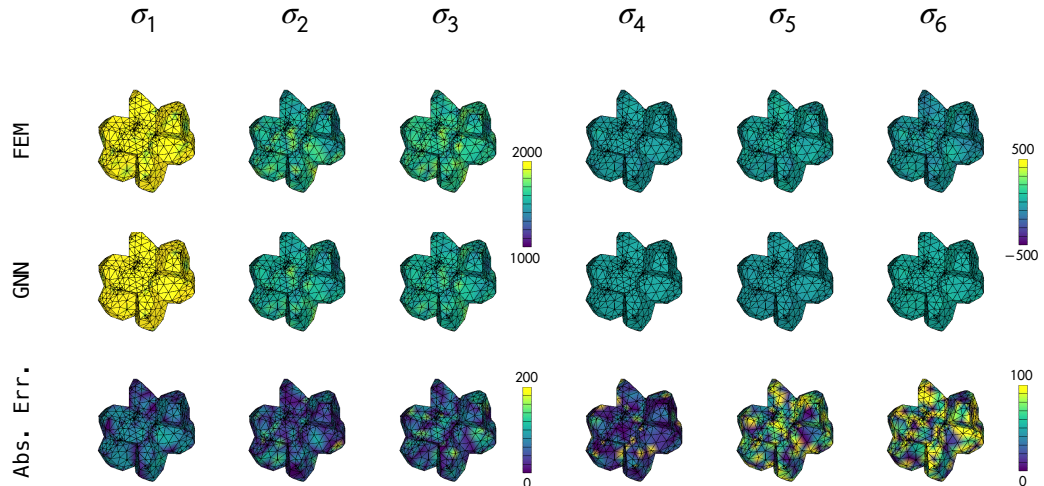


Figure 7: The comparison between FEM and GNN predictions, with absolute errors of stress components on one example grain in the testing sets. For the stress components coupled with 1-direction are visualized in the range [1000, 2000]. The corresponding absolute errors are visualized in the range [0, 200]. The uncoupled stress components are visualized in the range of [−500, 500]. The corresponding absolute errors are visualized in the range [0, 100]. The unit for stress is [MPa].

The von Mises's stresses are calculated on each cell as

$$\sigma_{\text{vM}} = \sqrt{\frac{1}{2} [(\sigma_1 - \sigma_4)^2 + (\sigma_4 - \sigma_6)^2 + (\sigma_6 - \sigma_1)^2 + 6(\sigma_2^2 + \sigma_3^2 + \sigma_5^2)]} \quad (23)$$

are visualized on the virtual polycrystals (Figure 8) comparing FEM and GNN, accompanied by the absolute errors. The general stress distribution

trends are well learned on the meshes, demonstrated by the stress data distribution. Figure 9 quantitatively verifies this observation with a high R^2 value of 0.94 and Pearson coefficient of 0.99. The overall MAE for the von Mises stress for this polycrystal is 56.63 [MPa], verifying and quantifying the low deviation of the GNN predictions from the benchmark. Combined analysis from Figure 7~9 detailedly illustrates GNN’s effective learning.

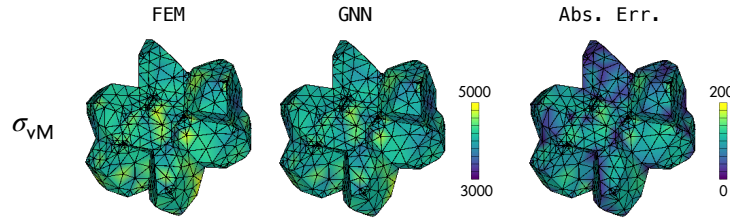


Figure 8: The comparison between FEM and GNN predictions (visualized in the range of [3000, 5000]), with absolute errors (visualized in the range of [0, 200]) on von Mises stress. The unit for stress is [MPa].

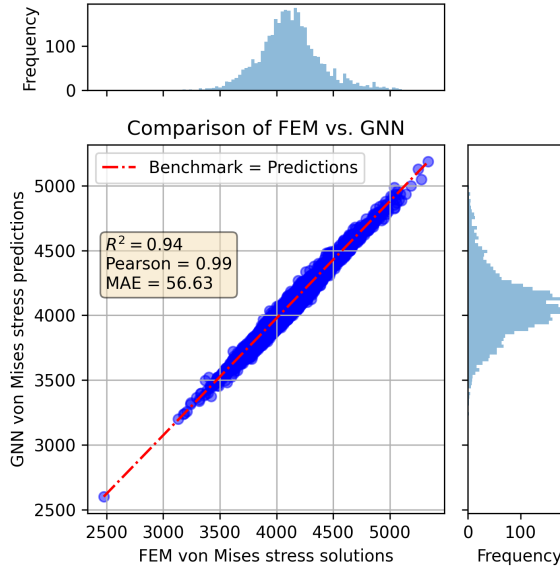


Figure 9: The evaluation of the prediction quality on von Mises stress for the example polycrystal. The unit for stress is [MPa].

Following the analysis procedure, we demonstrate the effective learning of the GNN by analyzing two other polycrystals with overall R^2 values of

0.992 and 0.991 from inferences, respectively (Figure 10 & 11). From the upper left figures, one observes very similar von Mises ranges are predicted by FEM and GNN, accompanied by low absolute errors. The quantitative comparison in the right figures confirms the qualitative observation for the von Mises stress inferences, with R^2 and Pearson coefficients of 0.96 and 0.99 for both the two polycrystals, respectively. Also, the two methods both predict similar stress component ranges demonstrated in the bottom left figures, illustrated by different color histograms. To summarize, these results demonstrate a few aspects of the robustness of the proposed GNN plasticity modeling: (1) overall stress components are predicted well by the high R^2 values, with no overfitting for testing sets; (2) general trends of stress components are captured; (3) von Mises stress are well learned verified both qualitatively and quantitatively, demonstrated via similar stress distribution and high R^2 and Pearson coefficients. Specifically, von Mises is not introduced (or constrained) in the training process. Additionally, the plasticity model is effectively learned from a limited amount of training data.

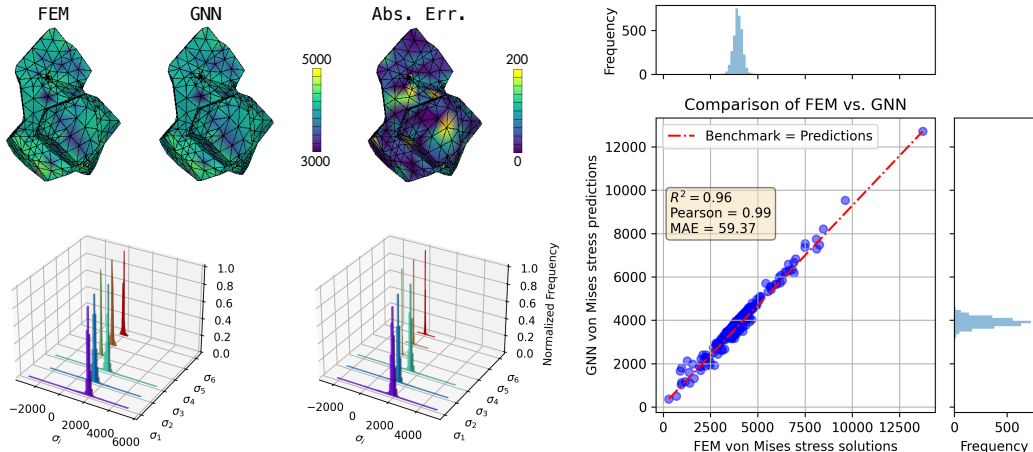


Figure 10: The evaluation of the prediction quality on von Mises stress for another example polycrystal. The upper left figures visualize the comparison between FEM and GNN predicted von Mises stress (plotted in range [3000, 5000]) and absolute errors (plotted in range [0, 200]). The bottom left figures visualize the distributions of different stress components. The right figure shows the direct map between FEM and GNN predicted von Mises stresses.

Figure 11 also reflects the potential limitation of the proposed method: the distribution of the stress components σ_4 , σ_5 , and σ_6 are not fully captured

by the GNN. Qualitatively, one may argue that the variance of the data distribution around zero is not learned via GNN. This can be explained by the low-stress value range for the related stress components uncoupled with the loading direction (i.e., 1-direction). However, as can be visually observed and with Eqn. (23), the stresses in the uncoupled directions do not significantly contribute to the von Mises stresses, considering the high-quality predictions on the von Mises stresses (Figs. 10 & 11). The stress components correlated to the loading direction match well with the benchmark as illustrated in the left-bottom figure.

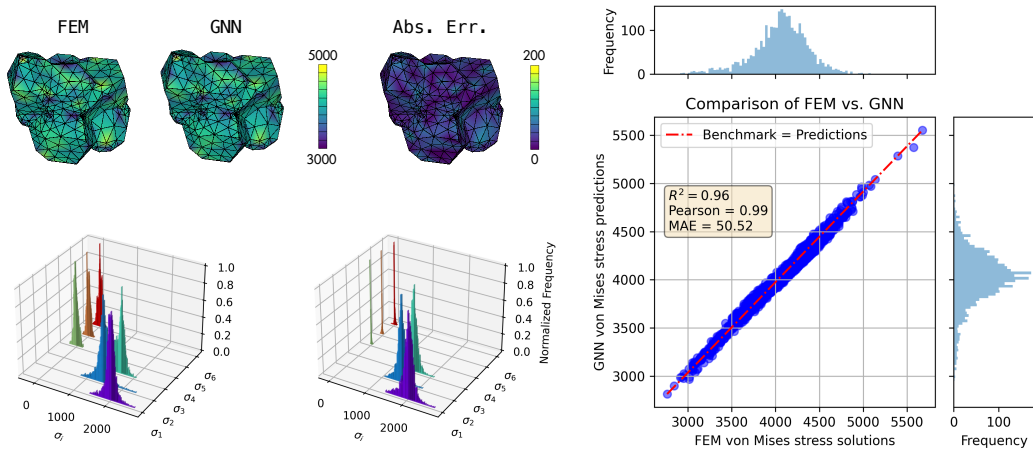


Figure 11: The evaluation of the prediction quality on von Mises stress for another example polycrystal. The upper left figures visualize the comparison between FEM and GNN predicted von Mises stress (plotted in range [3000, 5000]) and absolute errors (plotted in range [0, 200]). The bottom left figures visualize the distributions of different stress components. The right figure shows the direct map between FEM and GNN predicted von Mises stresses.

One of the main advantages of the proposed approach is to reduce the computational burden for plasticity modeling. Figure 12 presents the speed-up evaluation comparing the GNN and FEM methods by comparing the FEM and GNN computational time on 10 randomly selected polycrystals in the testing sets. From the subfigure, one observes that the time does not vary much for the 10 polycrystal samples (blue & red dots). The average speed-up is estimated to be 158, showing that the proposed GNN plasticity can significantly accelerate plasticity modeling with high-accuracy predictions. Several reasons could contribute to this speed-up: (i) In the FEM

model, the solver updates stress fields iteratively for each step. This involves nested loops to account for the nonlinear plasticity model, resulting in a significantly increased computational load [26]. (ii) The forward gradient evaluation is computationally efficient in PyTorch [31]. (iii) Our model size is compact (Eqn. (16) with small embedding size); this lightweight nature further contributes to the high-speed gradient evaluation mentioned in (ii).

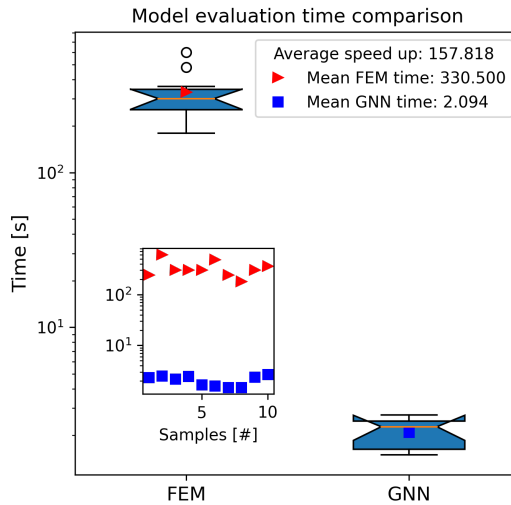


Figure 12: Speed up time comparing constitutive model evaluations of FEM and GNN from 10 randomly selected polycrystal samples. The models are evaluated on a single CPU node on the Sherlock system [32].

4.3. Deployment on unseen dataset

To thoroughly analyze the generalizability of the proposed GNN method, we extend our evaluation beyond the testing sets by running 30 entirely unseen simulations with newly generated polycrystals and estimating the prediction quality of the GNN. Figure 13 presents the overall predictions of stress components for the 30 unseen simulations, demonstrating accurate predictions with an R^2 value of 0.992 and a Pearson coefficient of 0.996. These results indicate that the proposed GNN method not only generalizes well within the provided training and testing sets (i.e., interpolation) but also effectively extrapolates to data outside the given data regime.

Figure 14 shows the comparison of the stress components predictions per cell for the overall ϵ - σ and ϵ_{11} - σ_{11} maps, respectively. The GNN inferences effectively preserve the stress data trends, including both the data distribution

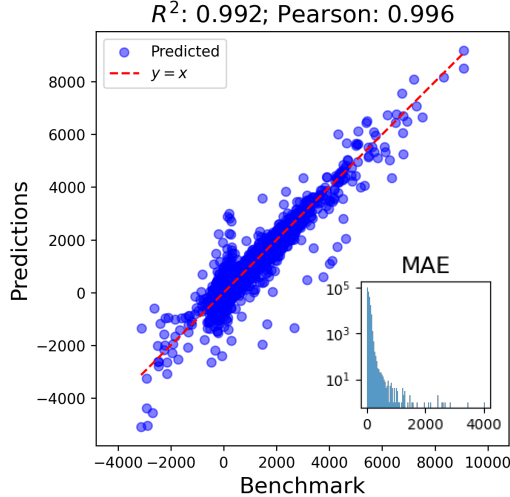


Figure 13: The overall prediction results on the unseen dataset and the absolute error distribution.

and the von Mises stress values. Interestingly, one may discern qualitatively higher discrepancies between the two methods in the “low-stress regime.” This observation aligns with the discussion on the limitations highlighted in Figure 11: the values for stress components around zero are not accurately captured. Nonetheless, the model demonstrates high performance and provides good predictions on the stress-strain maps overall.

Following a similar analytical procedure, Figures 15 and 16 present two analyses of previously unseen polycrystals. Both samples exhibit an overall R^2 value of 0.993 for stress components. The von Mises stresses are accurately predicted on the virtual polycrystals, as evidenced by both qualitative observations on the left and quantitative comparisons on the right, with high R^2 values of 0.94 and 0.96. Comparing these results with Figures 10-11, it can be deduced that the GNN plasticity method generalizes well beyond both training and testing sets, delivering similarly high-quality predictions on the polycrystals. We note that for both training, testing, and unseen datasets, the polycrystal meshes possess different dimensions. Conducting inference tests on these samples would be nearly impossible for traditional regression methods such as MLP or CNN.

Figure 17 presents an error analysis comparing the training and testing sets with the unseen datasets across all stress components (σ_1 to σ_6), by directly visualizing the MAE distribution. The distributions for the training

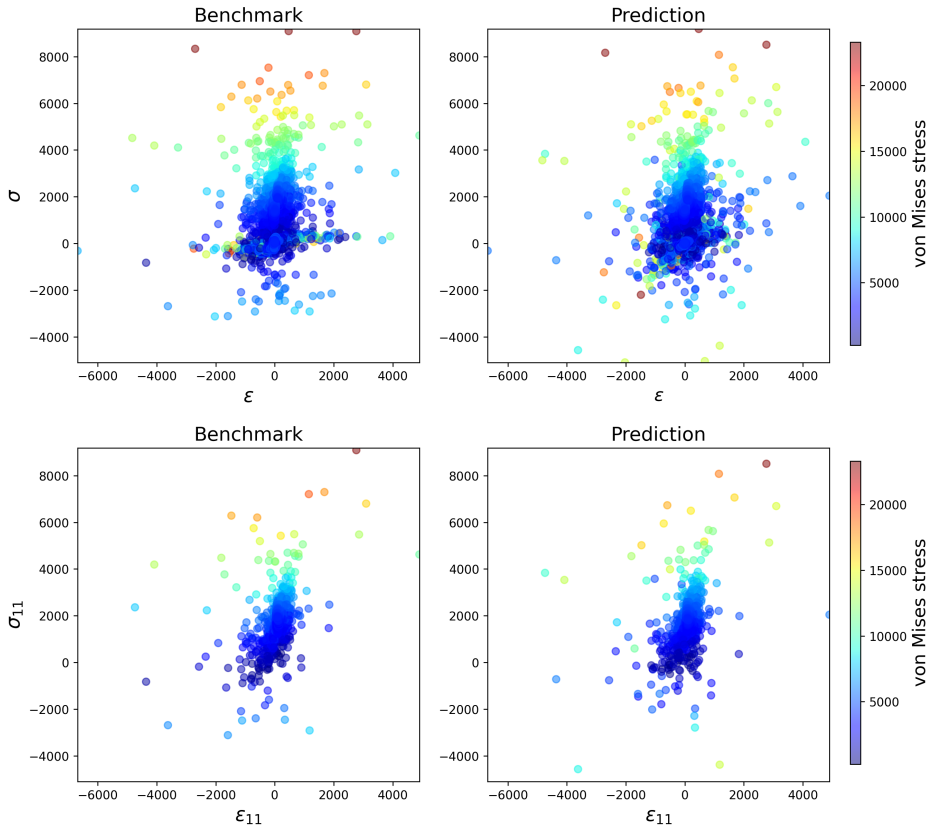


Figure 14: The comparison between the ground truth (by *FEpX*) and predictions on the stress-strain maps for all stress-strain components (top figures) and 1-direction (i.e., $\epsilon_{11} \rightarrow \sigma_{11}$) (bottom figures). The data points are visualized according to the calculated von Mises stresses.

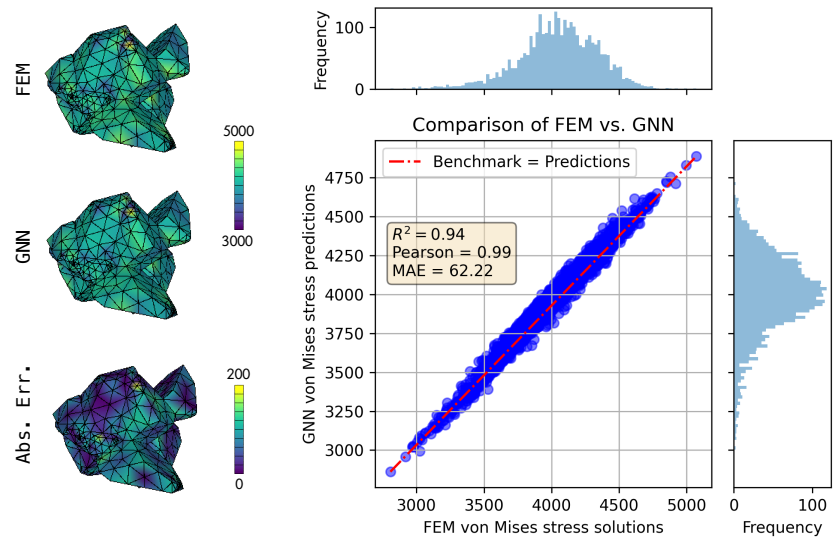


Figure 15: The evaluation of the prediction quality on von Mises stress for an example polycrystal in the unseen dataset. The left figures visualize the comparison between FEM and GNN predicted von Mises stress (plotted in range [3000, 5000]) and absolute errors (plotted in range [0, 200]). The right figure shows the direct map between FEM and GNN predicted von Mises stresses.

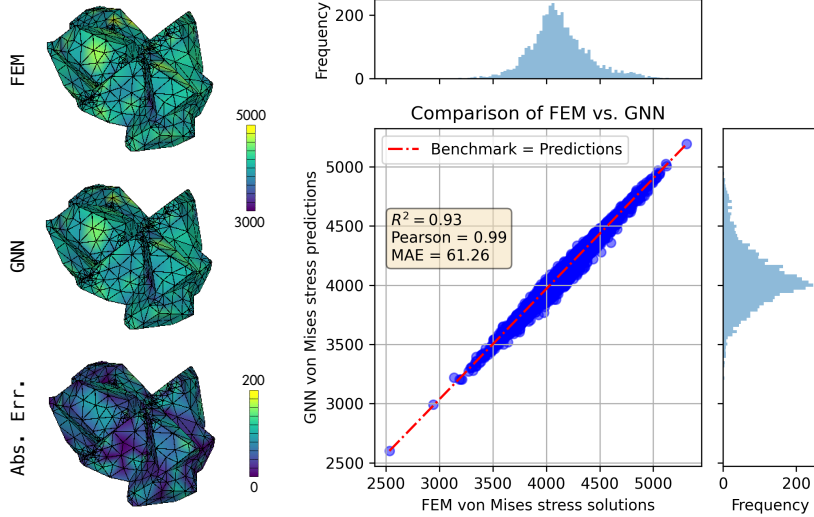


Figure 16: The evaluation of the prediction quality on von Mises stress for an example polycrystal in the unseen dataset. The left figures visualize the comparison between FEM and GNN predicted von Mises stress (plotted in range [3000, 5000]) and absolute errors (plotted in range [0, 200]). The right figure shows the direct map between FEM and GNN predicted von Mises stresses.

and testing sets closely resemble those of the unseen datasets, validating that the proposed GNN plasticity method does not overfit and generalizes well to the stress distributions across various polycrystals.

5. Summary and conclusions

In this paper, we introduce a novel approach to surrogate computational plasticity using graph neural networks with subgraph training. The key advantages of our method are: (1) Handling data with varying dimensions — our GNN model accommodates different node counts generated from various polycrystal meshes, allowing for flexible input data; (2) Efficient subgraph training — by randomly sampling subgraphs from polycrystals containing up to 10^5 nodes, we significantly reduce GPU memory requirements; (3) Preserving geometric features — our GNN model incorporates nodal and edge information, preserving the spatial distribution of stress and strain, thereby enhancing the “learnability” of the data.

Our numerical experiments demonstrate that the GNN model predicts stress components with high accuracy, achieving R^2 scores greater than

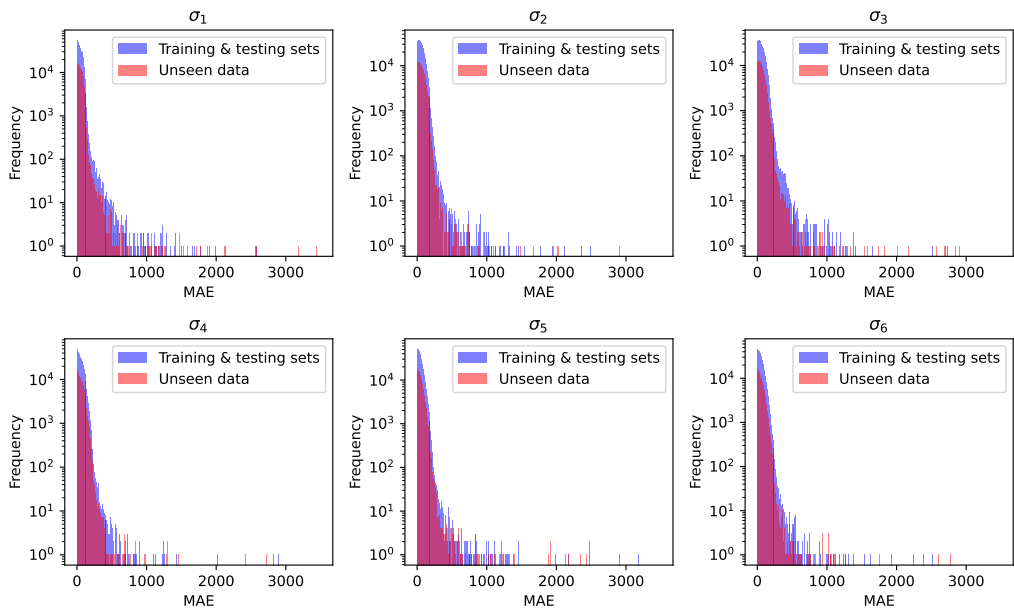


Figure 17: Comparison of absolute error distributions between the training & testing sets and unseen dataset.

0.99 on the training, testing, and unseen datasets. Additionally, the von Mises stress predictions for the polycrystals indicate that the proposed GNN method accurately captures von Mises stress features. The model generalizes well beyond the training and testing data, as evidenced by the similar MAE distribution across the training, testing, and unseen datasets.

We also briefly outline the limitations of our framework: stress components that are uncoupled from the loading direction are not accurately captured, as their values fluctuate around zero. However, this does not hinder the application of our method, as it does not lead to higher errors, and von Mises stress is still predicted accurately. These uncoupled stress components will not affect the effectiveness of this method when applied in mechanical analysis, particularly when estimating critical stress under plastic deformation.

This work is expected to lay the foundation for modeling polycrystal plasticity using GNNs and potentially inspire similar applications in other plasticity models. Future work could include incorporating physics-informed features into the framework and tackling more challenging plasticity modeling tasks, such as capturing time-dependent behaviors like cyclic loading.

Data Availability

The related codes are to be released via <https://gitlab.com/hanfengzhai2/GNN-FEM-PolyPlas>.

Acknowledgement

The author acknowledges support from the Enlight Foundation Graduate Fellowship via Leland Stanford Junior University.

References

- [1] R. von Mises, Mechanik der festen Körper im plastisch-deformablen Zustand, Nachrichten von der Gesellschaft der Wissenschaften zu Göttingen. Mathematisch-Physikalische Klasse 1913 (1913) 582–592.
- [2] M. T. Huber, Właściwa praca odkształcenia jako miara wyteżenia materiału, Czasopismo Techniczne 22 (1904).

- [3] A. Azushima, R. Kopp, A. Korhonen, D. Yang, F. Micari, G. Lahoti, P. Groche, J. Yanagimoto, N. Tsuji, A. Rosochowski, A. Yanagida, Severe plastic deformation (spd) processes for metals, *CIRP Annals* 57 (2008) 716–735. URL: <http://dx.doi.org/10.1016/j.cirp.2008.09.005>. doi:10.1016/j.cirp.2008.09.005.
- [4] E. Krempl, Design for Fatigue Resistance, volume 20, ASM International, 1997, p. 516–532. URL: <http://dx.doi.org/10.31399/asm.hb.v20.a0002469>. doi:10.31399/asm.hb.v20.a0002469.
- [5] T. Jiang, C. Wu, L. Spinella, J. Im, N. Tamura, M. Kunz, H.-Y. Son, B. Gyu Kim, R. Huang, P. S. Ho, Plasticity mechanism for copper extrusion in through-silicon vias for three-dimensional interconnects, *Applied Physics Letters* 103 (2013). URL: <http://dx.doi.org/10.1063/1.4833020>. doi:10.1063/1.4833020.
- [6] D. Hu, N. Grilli, W. Yan, Dislocation structures formation induced by thermal stress in additive manufacturing: Multiscale crystal plasticity modeling of dislocation transport, *Journal of the Mechanics and Physics of Solids* 173 (2023) 105235. URL: <http://dx.doi.org/10.1016/j.jmps.2023.105235>. doi:10.1016/j.jmps.2023.105235.
- [7] J. A. Mitchell, A Nonlocal, Ordinary, State-Based Plasticity Model for Peridynamics, Technical Report SAND2011-3166, Sandia National Laboratories, 2011.
- [8] D. C. Drucker, W. Prager, Soil mechanics and plastic analysis for limit design, *Quarterly of Applied Mathematics* 10 (1952) 157–165.
- [9] W. Dou, Z. Xu, H. Hu, F. Huang, A generalized plasticity model incorporating stress state, strain rate and temperature effects, *International Journal of Impact Engineering* 155 (2021) 103897. URL: <http://dx.doi.org/10.1016/j.ijimpeng.2021.103897>. doi:10.1016/j.ijimpeng.2021.103897.
- [10] R. B. Sills, N. Bertin, A. Aghaei, W. Cai, Dislocation networks and the microstructural origin of strain hardening, *Physical Review Letters* 121 (2018). URL: <http://dx.doi.org/10.1103/PhysRevLett.121.085501>. doi:10.1103/physrevlett.121.085501.

- [11] B. Luan, M. O. Robbins, Friction and plasticity in contacts between amorphous solids, *Tribology Letters* 69 (2021). URL: <http://dx.doi.org/10.1007/s11249-021-01429-7>. doi:10.1007/s11249-021-01429-7.
- [12] J. Chen, T. Furushima, Effects of intergranular deformation incompatibility on stress state and fracture initiation at grain boundary: Experiments and crystal plasticity simulations, *International Journal of Plasticity* 180 (2024) 104052. URL: <http://dx.doi.org/10.1016/j.ijplas.2024.104052>. doi:10.1016/j.ijplas.2024.104052.
- [13] H. F. Alharbi, S. R. Kalidindi, Crystal plasticity finite element simulations using a database of discrete fourier transforms, *International Journal of Plasticity* 66 (2015) 71–84. URL: <http://dx.doi.org/10.1016/j.ijplas.2014.04.006>. doi:10.1016/j.ijplas.2014.04.006.
- [14] A. Needleman, R. Asaro, J. Lemonds, D. Peirce, Finite element analysis of crystalline solids, *Computer Methods in Applied Mechanics and Engineering* 52 (1985) 689–708. URL: [http://dx.doi.org/10.1016/0045-7825\(85\)90014-3](http://dx.doi.org/10.1016/0045-7825(85)90014-3). doi:10.1016/0045-7825(85)90014-3.
- [15] S. Kalidindi, C. Bronkhorst, L. Anand, Crystallographic texture evolution in bulk deformation processing of fcc metals, *Journal of the Mechanics and Physics of Solids* 40 (1992) 537–569. URL: [http://dx.doi.org/10.1016/0022-5096\(92\)80003-9](http://dx.doi.org/10.1016/0022-5096(92)80003-9). doi:10.1016/0022-5096(92)80003-9.
- [16] Z. Yang, S. Papanikolaou, A. C. E. Reid, W.-k. Liao, A. N. Choudhary, C. Campbell, A. Agrawal, Learning to predict crystal plasticity at the nanoscale: Deep residual networks and size effects in uniaxial compression discrete dislocation simulations, *Scientific Reports* 10 (2020). URL: <http://dx.doi.org/10.1038/s41598-020-65157-z>. doi:10.1038/s41598-020-65157-z.
- [17] H. Salmenjoki, M. J. Alava, L. Laurson, Machine learning plastic deformation of crystals, *Nature Communications* 9 (2018). URL: <http://dx.doi.org/10.1038/s41467-018-07737-2>. doi:10.1038/s41467-018-07737-2.

- [18] M. Mińkowski, L. Laurson, Predicting elastic and plastic properties of small iron polycrystals by machine learning, *Scientific Reports* 13 (2023). URL: <http://dx.doi.org/10.1038/s41598-023-40974-0>. doi:10.1038/s41598-023-40974-0.
- [19] Z. Yang, M. J. Buehler, Linking atomic structural defects to mesoscale properties in crystalline solids using graph neural networks, *npj Computational Materials* 8 (2022). URL: <http://dx.doi.org/10.1038/s41524-022-00879-4>. doi:10.1038/s41524-022-00879-4.
- [20] N. Amigo, S. Palominos, F. J. Valencia, Machine learning modeling for the prediction of plastic properties in metallic glasses, *Scientific Reports* 13 (2023). URL: <http://dx.doi.org/10.1038/s41598-023-27644-x>. doi:10.1038/s41598-023-27644-x.
- [21] M. Dai, M. F. Demirel, Y. Liang, J.-M. Hu, Graph neural networks for an accurate and interpretable prediction of the properties of polycrystalline materials, *npj Computational Materials* 7 (2021). URL: <http://dx.doi.org/10.1038/s41524-021-00574-w>. doi:10.1038/s41524-021-00574-w.
- [22] Z. Fan, E. Ma, Predicting orientation-dependent plastic susceptibility from static structure in amorphous solids via deep learning, *Nature Communications* 12 (2021). URL: <http://dx.doi.org/10.1038/s41467-021-21806-z>. doi:10.1038/s41467-021-21806-z.
- [23] A. Thomas, A. R. Durmaz, M. Alam, P. Gumbsch, H. Sack, C. Eberl, Materials fatigue prediction using graph neural networks on microstructure representations, *Scientific Reports* 13 (2023). URL: <http://dx.doi.org/10.1038/s41598-023-39400-2>. doi:10.1038/s41598-023-39400-2.
- [24] S. Yee Tung, Tan Ee Siang, Influence of curing agent on thermal conductivity and mechanical properties of epoxy composite with silicon nitride nanofillers, *IOP Conference Series: Materials Science and Engineering* 1284 (2023) 012052. doi:10.1088/1757-899X/1284/1/012052.
- [25] W. Huang, J.-Y. Zhu, C.-Y. Song, L. Sun, J.-P. Zheng, Mesh-based gnn surrogates for time-independent pdes, *Scientific Reports* 14 (2024) 53185. doi:10.1038/s41598-024-53185-y.

- [26] R. Quey, P. Dawson, F. Barbe, Large-scale 3d random polycrystals for the finite element method: Generation, meshing and remeshing, *Computer Methods in Applied Mechanics and Engineering* 200 (2011) 1729–1745. URL: <http://dx.doi.org/10.1016/j.cma.2011.01.002>. doi:10.1016/j.cma.2011.01.002.
- [27] P. R. Dawson, D. E. Boyce, Fepx – finite element polycrystals: Theory, finite element formulation, numerical implementation and illustrative examples, 2015. URL: <https://arxiv.org/abs/1504.03296>. doi:10.48550/ARXIV.1504.03296.
- [28] E. C. Aifantis, The physics of plastic deformation, *International Journal of Plasticity* 3 (1987) 211–247. URL: [http://dx.doi.org/10.1016/0749-6419\(87\)90021-0](http://dx.doi.org/10.1016/0749-6419(87)90021-0). doi:10.1016/0749-6419(87)90021-0.
- [29] C.-S. Han, H. Gao, Y. Huang, W. D. Nix, Mechanism-based strain gradient crystal plasticity—i. theory, *Journal of the Mechanics and Physics of Solids* 53 (2005) 1188–1203. URL: <http://dx.doi.org/10.1016/j.jmps.2004.08.008>. doi:10.1016/j.jmps.2004.08.008.
- [30] R. Quey, M. Kasemer, The neper/fepx project: Free / open-source polycrystal generation, deformation simulation, and post-processing, *IOP Conference Series: Materials Science and Engineering* 1249 (2022) 012021. URL: <http://dx.doi.org/10.1088/1757-899X/1249/1/012021>. doi:10.1088/1757-899X/1249/1/012021.
- [31] A. Paszke, S. Gross, S. Chintala, G. Chanan, E. Yang, Z. DeVito, Z. Lin, A. Desmaison, L. Antiga, A. Lerer, Automatic differentiation in PyTorch, in: *NIPS 2017 Workshop Autodiff*, 2017, pp. –. URL: <https://openreview.net/forum?id=BJJsrmfCZ>, 28 Oct 2017 (modified: 28 Oct 2017).
- [32] S. University, Sherlock cluster documentation, 2024. URL: <https://www.sherlock.stanford.edu/docs>, accessed: 2024-08-05.